OPEN ACCESS

Onset Shift of Li Plating on Si/Graphite Anodes with Increasing Si Content

Journal of The Electrochemical Society, 2023 **170** 060536

Onset Shift of Li Plating on Si/Graphite Anodes with Increasing Si Content

Marius Flügel,[1] Marius Bolsinger,[2] Mario Marinaro,[1] Volker Knoblauch,[2] Markus Hölzle,[1] Margret Wohlfahrt-Mehrens,[1,3] and Thomas Waldmann[1,3,z]

[1]*Zentrum für Sonnenenergie- und Wasserstoff-Forschung Baden-Württemberg (ZSW), D-89081 Ulm, Germany*
[2]*Aalen University of Applied Sciences (AU), Materials Research Institute, D-73430 Aalen, Germany*
[3]*Helmholtz Institute Ulm for Electrochemical Energy Storage (HIU), Helmholtzstraße 11, D-89081 Ulm, Germany*

Mixing graphite with Si particles in anodes of Li-ion batteries provides increased specific energy. In addition, higher Si contents lead to thinner anode coatings at constant areal capacity. In the present study, we systematically investigated the influence of the Si content on the susceptibility of Li plating on Si/graphite anodes. Si/graphite anodes with Si contents from 0 to 20.8 wt% combined with NMC622 cathodes were manufactured on pilot-scale. After initial characterization in coin half cells and by SEM, pouch full cells with fixed N/P ratios were built. Rate capability at different temperatures, and Post-Mortem analysis were carried out. Results from voltage relaxation, Li stripping, SEM measurements, glow discharge optical emission spectroscopy (GD-OES) depth profiling, and optical microscopy were validated against each other. A decreasing susceptibility to Li plating with increasing Si content in the anodes could be clearly observed. A critical C-rate was defined, at which Li plating was detected for the first time. It was also found that at 0 °C the critical C-rate increases with increasing Si contents. At 23 °C the SOC at which Li dendrites were first observed on the anode also increased with higher Si content.

 [DOI: 10.1149/1945-7111/acdda3]

Manuscript submitted February 23, 2023; revised manuscript received May 25, 2023. Published June 22, 2023.

Since the initial days of Li-ion batteries, the specific anode capacity was limited to a theoretical value of 372 mAh g^{-1},[1] as graphite was the only material of choice and can only reversibly store one Li atom per six C atoms. Silicon as an anode material, however, allows the storage of nearly four Li atoms per Si atom in $Li_{15}Si_4$, resulting in a theoretical capacity of 3,579 mAh g^{-1} at room temperature.[2] However, the highest possible alloying level of Si is accompanied by a strong volume expansion of almost 300%,[3] which leads to particle cracking, repeated SEI formation, and even electrode delamination.[4–6] Blending lower amounts with Si with graphite is one elegant way to mitigate these issues.[7–10]

Recent studies have proven that Si compounds are already incorporated in the anodes of commercially available cells.[11,12] After the method development by Richter et al., it became possible to determine the Si content with glow discharge optical emission spectroscopy (GD-OES) depth profiling measurements of anodes from Post-Mortem analysis.[13,14] Our recent study with Post-Mortem analysis of 18 cylindrical cells showed that commercial cells contain up to 4 wt% Si in the anode.[15] Si compounds in the anode can either lead to higher specific energy when the thickness of the electrode is kept constant or to thinner anode coatings at the same anode areal capacity.[15] For example, the anode coating thickness at a desired energy density of 190 Wh kg^{-1} can be reduced from 80 μm for a pure graphite coating to 53 μm in case of a Si/graphite coating with 3.5 wt% Si. Alternatively, the specific energy can be increased from 160 to 190 Wh kg^{-1} at a constant anode thickness of 53 μm by increasing the Si content from 0.8 wt% to 3.5 wt%.[15]

Studies on the aging mechanisms of Si/graphite anodes have identified either loss of anode active material (LAAM)[13,15–17] or loss of Li inventory (LLI) as main causes of capacity loss.[15,18–20] LAAM can occur during particle fracture and electronic isolation of Si particles by an excessively thick SEI. LLI often takes place simultaneously due to Li being stuck in fractured or isolated particles as a result of Li consumption in the SEI.[21,22]

As of today, few studies had been performed on Li plating on Si/graphite anodes,[15,23] what basically might be a similar process compared to pure graphite anodes at low temperatures and high charge rates.[24] Using neutron diffraction experiments and cells that suffered from Li plating, Richter et al. found that deposited Li first is re-intercalating into graphite before redistributing from graphite into Si.[23] We investigated the Li plating conditions of several cylindrical Si containing cells, which were classified as high-energy or high-power cells.[15] Si/graphite anodes in high-energy cells show a stronger susceptibility to Li plating compared to high-power cells due to their higher coating thickness and lower porosity.[15] Furthermore, we found that the tendency for Li plating increases after aging when LAAM in the form of loss of the Si compound is the main aging mechanism.[15] Similarly, in case of LLI as main aging mechanism, the susceptibility to Li plating decreases.[15]

Since Li plating presents a significant safety risk due to internal short circuits[25,26] and lower onset temperatures for exothermic reactions and the thermal runaway,[27,28] identifying Li plating in an early stage is essential for safe battery operation. Several literature reviews have already been published summarizing the established methods for in situ and Post-Mortem detection of Li plating.[24,29,30] In situ methods for Li plating metal detection are the use of a reference electrode between anode[31,32] and cathode as well as observing the voltage relaxation profile (VRP) after charging.[33,34] At anode potentials below 0 V vs Li/Li^+, Li plating is thermodynamically favored over Li intercalation into the active material.[35] Once Li plating has occurred, Li metal can re-intercalate into the anode, thus keeping the anode potential constant and resulting in a flat voltage plateau.[33,34]

Post-Mortem methods for detection of Li plating on anodes in disassembled cells include XPS,[36] GD-OES[15,28,37] and SEM.[28,38] The minimum amount of metallic Li can be quantified on graphite[37] and Si/graphite anodes[15] using GD-OES. Li plating can be qualitatively detected by SEM due to the characteristic dendrites.[38,39]

In this study, we investigate changes in Li plating on anodes with increasing Si content. Anodes were coated with identical areal capacity, resulting in lower coating thickness at higher Si contents. Higher irreversible capacities of anodes with higher Si content were compensated by higher areal capacities of the cathode. Since the N/P ratio, defined as the ratio of the areal capacity of the anode relative to the cathode, also influences the occurrence of Li plating, the required cathode capacities were selected in a way that all cells have an N/P ratio of 1.1. Furthermore, this study includes a method validation for voltage relaxation, Li stripping, SEM measurements, and GD-OES depth profiling. Another aim of this study is to reveal general trends on aging and susceptibility to Li plating.

[z]E-mail: thomas.waldmann@zsw-bw.de

Experimental

Electrode manufacturing.—Graphite active material and four Si/graphite composite active materials with different Si contents were purchased from Iopsilion (China). The Si content in the active material was 0 wt% (Graphite), 3.2 wt% (SiG3.0), 3.7 wt% (SiG3.5), 6.2 wt% (SiG5.8) and 23.1 wt% (SiG20.8), as determined with total carbon (TC)-analysis. Anode coatings were prepared using active material, CMC binder (TIMCAL, Switzerland), SBR binder (ZEON, Japan), and SuperC65 conductive additive (Nippon paper Industries, Japan) with a weight ratio of 94:2:2:2 (Graphite, SiG3.0—SiG5.8) and 90:3:3:4 (SiG20.8).

A 2 wt% binder solution was prepared in a planetary mixer in which carbon black firstly was homogenized before adding active material and SBR. The anode slurry was coated onto Cu foil using a pilot coater a width of 80 mm at a speed of 1.5 m min^{-1}. Calendering to a target density of 1.3 g cm^{-3} was done at roll temperatures of 40 °C.

Cathode coatings are prepared by coating N-methyl pyrrolidone (NMP) based slurries with 94 wt% active material (BASF, Germany), 2 wt% PVDF (Solvay, Belgium), 2 wt% carbon black (TIMCAL, Switzerland), and 2 wt% graphite (TIMCAL, Switzerland) onto Al foil. The cathodes were calendered at 100 °C roll temperature to a density of 3.2 g cm^{-3}.

Electrode compositions and active material loadings are summarized in Table I.

Cell manufacturing.—Reversible and irreversible capacities of the electrodes were determined with CR2032 coin half cells at ZSW. They were built with a 12 mm diameter working electrode, 2 layers of separator (Whatman, GF/A), and a 16 mm diameter Li counter electrode. Graphite cells were filled with 150 μl of 1 M $LiPF_6$ in EC: DEC (3: 7 wt%) + 2 wt% VC (Gotion, USA) and Si containing cells were filled with 150 μl of 1 M $LiPF_6$ in EC: DEC (3: 7 wt%) + 10 wt% FEC (Gotion, USA). Graphite and Si/Gr coin half cells were operated in the voltage window of 0.01–1.5 V and NMC622 coin half cells in the voltage window of 3.0–4.3 V.

Pouch full cell were assembled at ZSW using one double-sided coated anode with an area of 26 cm^2 and two single-sided coated cathodes with an area each of 24 cm^2, and Celgard 2325 separator. Graphite pouch full cells were filled with 1.5 mL of VC or FEC containing electrolyte and Si pouch cells were filled with 1.5 mL of FEC containing electrolyte. The pouch full cells were operated in the voltage window of 3.0–4.2 V.

Cells used for ex situ light microscopy imaging at Aalen University of Applied Sciences (AU) were built in an Ar-filled glove box (GS Glovebox Systemtechnik; <1.0 ppm O_2 & <1.0 ppm H_2O). The half cell setup consists of a 15 mm diameter anode mm and a 14 mm diameter Li foil electrode (Sigma Aldrich, 750 μm thickness), with a 16 mm diameter GF/A separators and a Celgard 2325 in between. 150 μl electrolyte (1 M $LiPF_6$ in EC: DEC (3: 7 wt %) + 10% FEC) was added to each coin cell.

Electrochemical tests.—EIS measurements to determine the tortuosity were performed on a BioLogic VMP 3 in a symmetrical coin cell set-up at room temperature. The EIS measurements were performed in multi-sine mode within a frequency range of 500 kHz to 10 mHz with a sinusoidal potential amplitude of 10 mV. Tortuosity values were calculated by fitting of the experimental data using ZView (Scribner Associates, Inc.). The symmetrical setup was used to avoid a mixed impedance between different working and counter electrodes and to simulate blocking conditions. Electrodes from the same anode with an area of 1.131 cm^{-2} and 2.011 cm^{-2} were punched out and dried 16 h under vacuum at 130 °C. The coin cells were then assembled in an argon filled glovebox using two layers of GF/A and 150 μl of electrolyte. Graphite cells were filled with 150 μl of 1 M $LiPF_6$ in EC: DEC (3 : 7 wt%) + 2 wt% VC and Si containing cells were filled with 150 μl of 1 M $LiPF_6$ in EC: DEC (3 : 7 wt%) + 10 wt% FEC.

The electrochemical measurements were conducted with MACCOR systems and cells positioned in climate chambers (CTS). The formation cycles started after 12 h soaking time by charging at 0.1 C to 4.2 V in CC–CV (constant current - constant voltage) mode and discharging at 0.1 C to 3.0 V in CC mode. During charge rate capability tests the cells were charged three times in CC mode to 4.2 V at charging rates of 0.1 C, 0.2 C, 0.33 C, 0.5 C, 1 C, 1.5 C, and 2 C. After reaching 4.2 V, the cells rested for 1 h (Si/graphite cells) or 3 h (Graphite cells) before discharged at 0.2 C to 3.0 V. All tests were performed with 3 cells each at 25 °C ± 1 °C and at 0 °C.

The amount of Li deposited on the anodes was quantified by fully charging two cells of each cell type in CC mode at 0 °C and immediately discharging the cells at 0.05 C to 3.0 V. The capacity charged into the cells at each C-rate is equal to the capacity charged into the cells at 0.1 C (CC) to 4.2 V. Metal plates were attached to the cells for better heat dissipation.

For a short aging of 5 cycles, 2 cells of each cell type were charged at 0 °C at 0.2 C and 0.33 C (graphite), 0.33 C and 0.5 C (SiG3.0 and SiG3.5), and 0.5 C and 1 C (SiG5.8 and SiG20.8), respectively, and discharged at 0.2 C.

Testing of the half cells for ex situ light microscopy was done with a BASYTEC CTS-Lab battery tester and all cells were set up in a climate chamber (Binder) at 23 °C. Formation was conducted by three charge / discharge cycles at a current rate of C/10. Charging was performed in CC-CV mode and discharging in CC mode. The half cells were cycled between 1.5 V and 0.01 V. Lithiation is terminated by reaching the <C/40 criteria. The theoretical capacity based on the electrodes mass loading was used for the charge and discharge current calculations. After formation, the cells were charged in CC mode with 1 C to different SOCs (50%–100%).

Table I. Summary of physico-chemical anode properties.

	Graphite	SiG3.0	SiG3.5	SiG5.8	SiG20.8
Si in AM	0 wt%	3.2 wt%	3.7 wt%	6.2 wt%	23.1 wt%
AM	94 wt%	94 wt%	94 wt%	94 wt%	90 wt%
CB	2 wt%	2 wt%	2 wt%	2 wt%	4 wt%
CMC	2 wt%	2 wt%	2 wt%	2 wt%	3 wt%
SBR	2 wt%	2 wt%	2 wt%	2 wt%	3 wt%
Si in Anode	0 wt%	3.0 wt%	3.5 wt%	5.8 wt%	20.8 wt%
AM Loading Anode	8.7 mg cm^{-2}	7.7 mg cm^{-2}	7.4 mg cm^{-2}	6.9 mg cm^{-2}	5.3 mg cm^{-2}
AM Loading Cathode	15.4 mg cm^{-2}	15.9 mg cm^{-2}	16.5 mg cm^{-2}	17.1 mg cm^{-2}	19.3 mg cm^{-2}
Density	1.3 g cm^{-3}	1.3 g cm^{-3}	1.3 g cm^{-3}	1.3 g cm^{-3}	1.3 g cm^{-3}
Porosity	42.4 ± 0.3%	43.5 ± 0.1%	44.1 ± 0.2%	42.7 ± 0.2%	42.9 ± 0.1%
Tortuosity	7.92	6.08	7.57	7.04	6.71
D_{50} value	14.77 μm	14.50 μm	14.12 μm	13.18 μm	13.16 μm

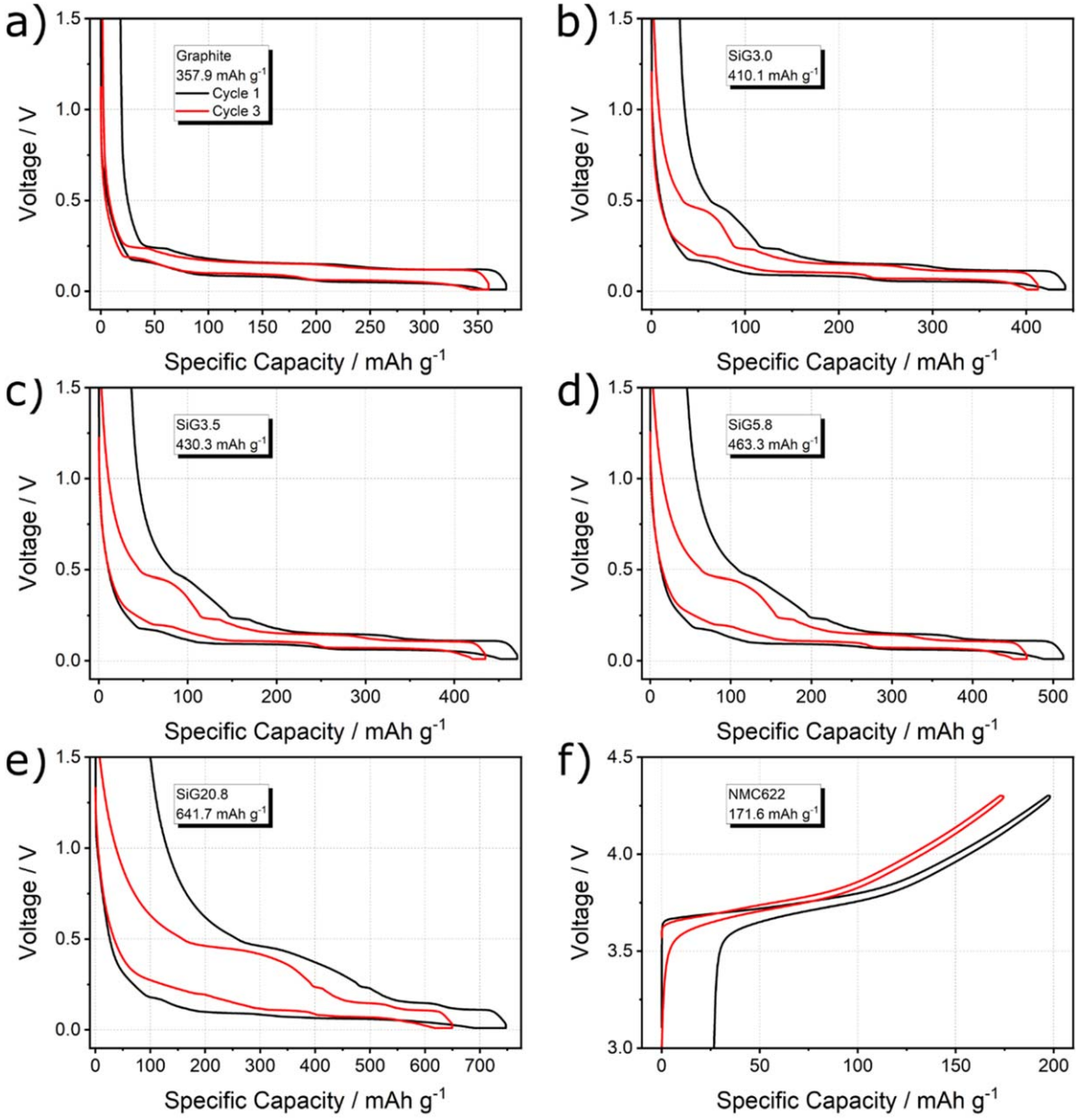

Figure 1. (a)–(e) Voltage profiles of the five anodes and (f) the NMC622 cathode showing the first formation cycle in black and the third formation cycle in red. The discharge capacity of the third formation cycle is shown in the box below the electrode name.

Post-mortem characterization.—GD-OES depth profiling analyses were conducted at ZSW using a GDA750 measurement device (Spectruma, Germany). The measurements were performed in radio frequency (RF) mode at a frequency of 2501 Hz, at a discharge voltage of 550 V and a pressure of 2 hPa. A mixture of 1% H_2 in Ar (both 6.0 purity) was used as sputtering gas. The following specific emission lines for individual elements were used for detection: H (121.6 nm), O (130.2 nm), C (156.1 nm), P (178.3 nm), Si (288.1 nm), Li (670.7 nm).

Scanning electron microscopy (SEM) of electrodes was performed with a secondary electron (SE) detector at 5 kV using a LEO 1530 VP (Zeiss) equipped with a Gemini thermal field emission column at ZSW. Cross-sections of anodes were generated with a Hitachi IM4000Plus broad-beam argon ion milling system, using an ion beam voltage of 5 kV. During sample preparation for SEM (top view and cross-section), the samples were exposed to air.

For Hg porosimetry measurements at ZSW, a 20 cm long electrode piece was used and a double determination of porosity was performed. Hg porosimetry was performed using a PASCAL 140–440 Series from Porotec. The pressure was slowly increased until the instrument detected Hg intrusion into the sample. The pressure increase was then reduced and stopped until Hg intrusion has taken place. Afterwards, the pressure was increased again and the process was repeated. The pressure was increased at 6–19 MPa min^{-1} up to a maximum pressure of 374 MPa.

High-resolution light microscopy was performed with a ZEISS Axio Observer 7 with an EC Epiplan-Neofluar 100x objective using a neutral white (3200 K) LED and an extended depth of field mode inside the glovebox at AU. The images were taken in the center of the electrode.

Results and Discussion

Electrode and cell characterization.—For this work, we purchased four already blended Si/graphite powders as well as the pure graphite powder used in the blends with Si. The specific capacities of the active materials were listed by the manufacturer as 355 mAh g^{-1} (Graphite), 400 mAh g^{-1} (SiG3.0), 420 mAh g^{-1} (SiG3.5), 450 mAh g^{-1} (SiG5.8) and 650 mAh g^{-1} (SiG20.8).[40] The particle size

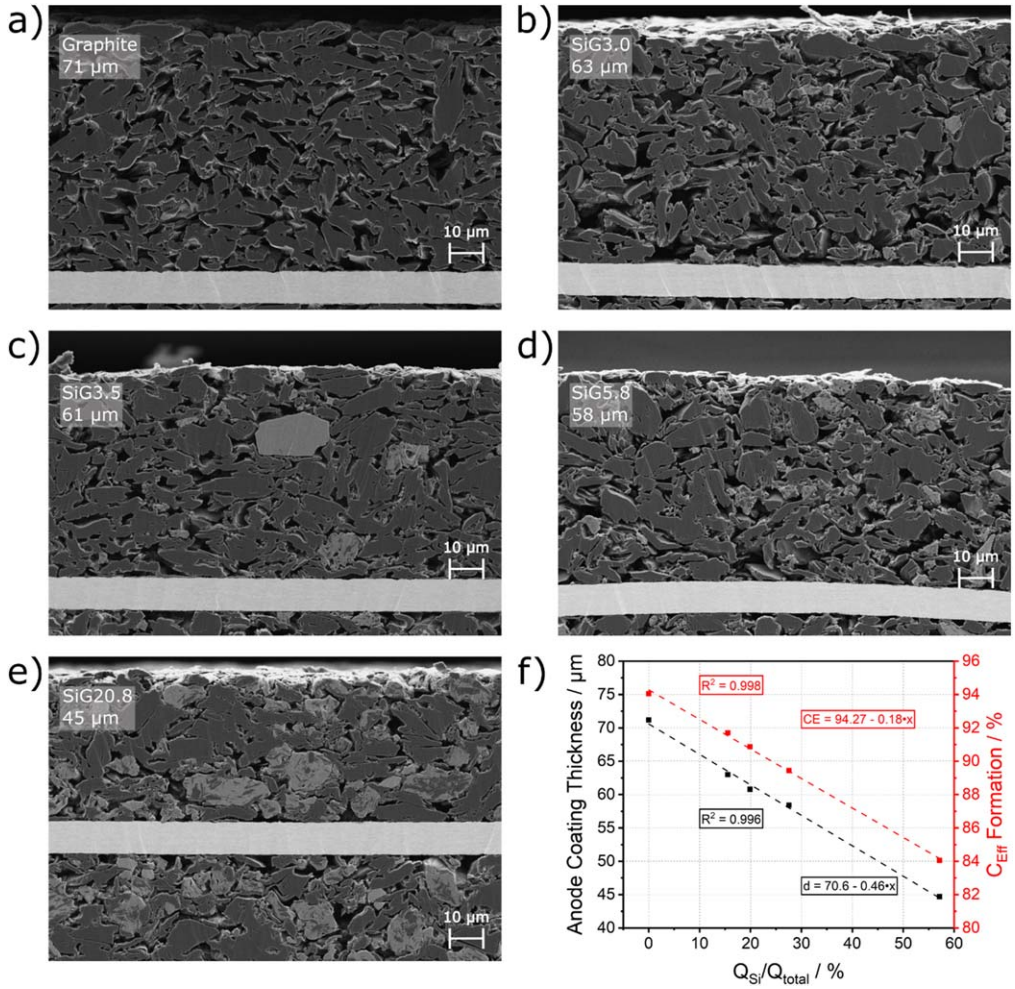

Figure 2. (a)–(e) SEM images of one side of the double-sided anodes taken with the SE detector; (f) plot of the anode coating thickness vs. Si capacity contribution (black) and initial coulombic efficiency vs Si capacity contribution (red).

Table II. Summary of electrochemical cell properties, which were determined experimentally in half cells as well as the theoretical capacity specified by the manufacturer. The reported irreversible capacity includes the irreversible capacity losses of all three formation cycles.

	NMC622	Graphite	SiG3.0	SiG3.5	SiG5.8	SiG20.8
Theoretical Capacity specified by the manufacturer [mAh g^{-1}]		355	400	420	450	650
Reversible Capacity [mAh g^{-1}]	171.6	357.9	410.1	430.3	463.3	641.7
Irreversible Capacity [mAh g^{-1}]	26.5	22.6	37.1	43.3	54.7	121.2
C_{eff} Formation [%]	86.62	94.05	91.70	90.87	89.44	84.06
Areal Capacity [mAh cm^{-2}]	2.63–3.30	3.11	3.16	3.18	3.20	3.40
N/P Ratio [-]		1.10	1.11	1.10	1.09	1.13
Q_{Si}/Q_{total} [%]		0	15.52	19.90	27.54	57.11

distribution reveals that the D_{50} value (Table I) of the powder mixtures decreases with higher Si content, which is in agreement with the SEM observations. However, SEM investigations have also revealed that the Si microparticles are secondary particles consisting of Si nanoparticles in a C matrix. By TC analysis, the Si content was determined to be 3.2 wt% Si (SiG3.0), 3.7 wt% Si (SiG3.5), 6.2 wt% (SiG5.8), and 23.1 wt% (SiG20.8) of the respective active material.

The porosities of the anodes were determined by Hg intrusion and the tortuosity by EIS. The values listed in Table I are very similar, and therefore effects of differences in porosity or tortuosity on fast-charge capability and Li plating can be excluded in this study.

Figure 1 shows the cell voltage during the first (black line) and third (red line) lithiation and de-lithiation cycle. As expected, the experimental specific capacity of the anode increases with the amount of Si in the anode due to its higher specific capacity. Experimentally determined irreversible capacity losses also increase with the amount of Si in the anode, which is consistent with literature and the intrinsically higher first cycle capacity loss of Si.[41] The irreversible capacities refer to the total irreversible losses of the three formation cycles. All experimental reversible and irreversible capacities are listed in Table II. The voltage profiles of the different anodes are comparable during lithiation. However, during de-lithiation the voltages of the cells with Si-containing anodes are higher, most likely due to the hysteresis of Si.[42]

We used the Si mass fractions ω of the respective active materials as well as the specific capacities q to calculate the overall capacity contribution of Si (Q_{Si}/Q_{total}) to the anode active material (Table II)

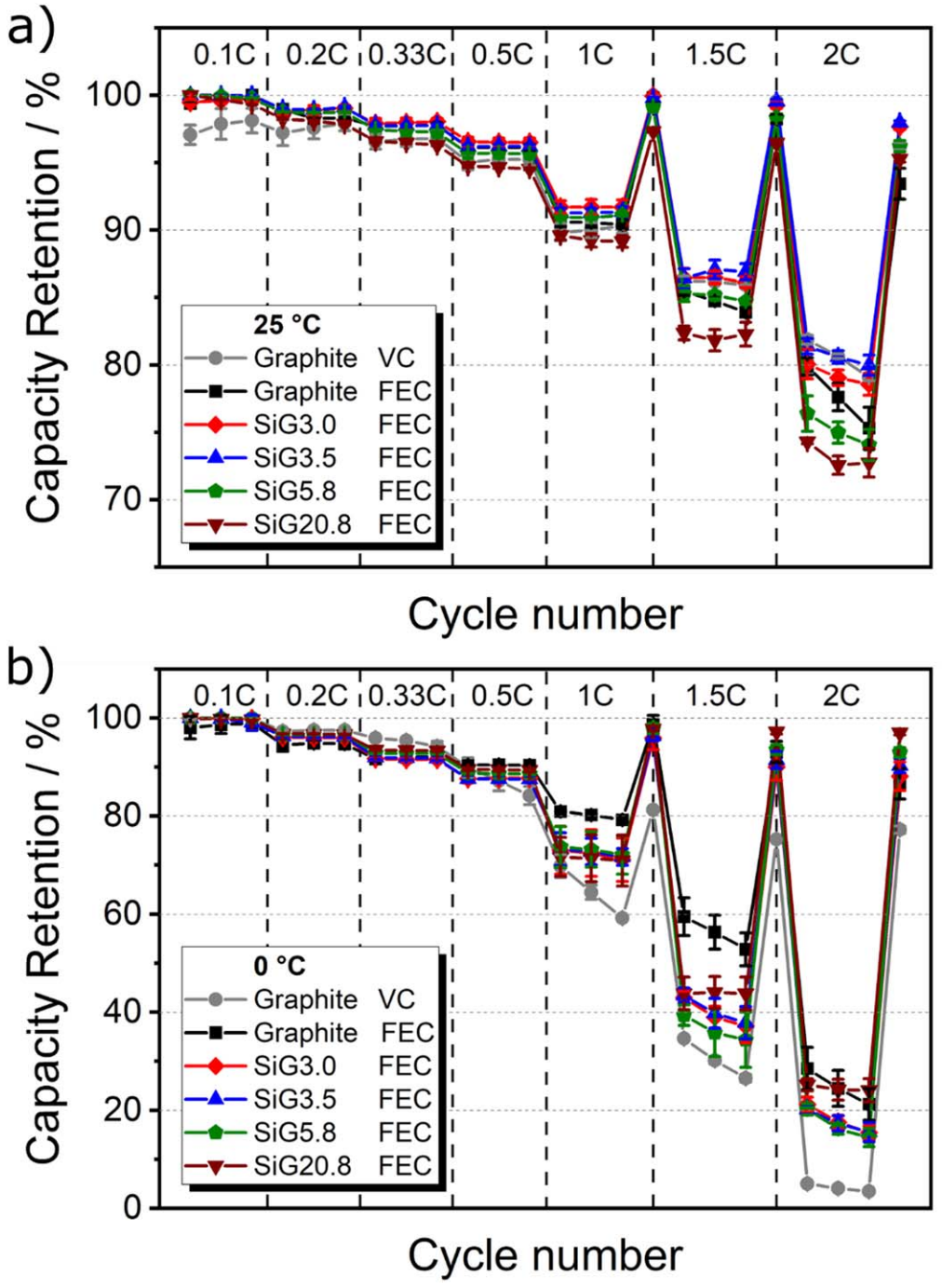

Figure 3. Charge rate capability tests at (a) 25 °C and (b) 0 °C, in which the cells were charged to 4.2 V in CC mode and discharged at 0.2 C to 3.0 V. After charging three times at 1 C, 1.5 C, and 2 C, a check-up cycle at 0.1 C was inserted.

Table III. Capacity charged into the cells at 0.1 C (CC) to 4.2 V (row 1) and the capacities obtained from the dissolution of the deposited Li during discharge at 0.05 C. The first column gives the charging C-rate.

	Graphite 10% FEC	SiG3.0 10% FEC	SiG3.5 10% FEC	SiG5.8 10% FEC	SiG20.8 10% FEC
Charged Capacity	103 mAh	107 mAh	108 mAh	113 mAh	115 mAh
0.2 C	0 mAh	0 mAh	0 mAh	0 mAh	0 mAh
0.33 C	0.7 mAh	0 mAh	0 mAh	0 mAh	0 mAh
0.5 C	3.6 mAh	1.4 mAh	0.7 mAh	0.7 mAh	0 mAh
1 C	7.6 mAh	4.4 mAh	3.9 mAh	3.5 mAh	—

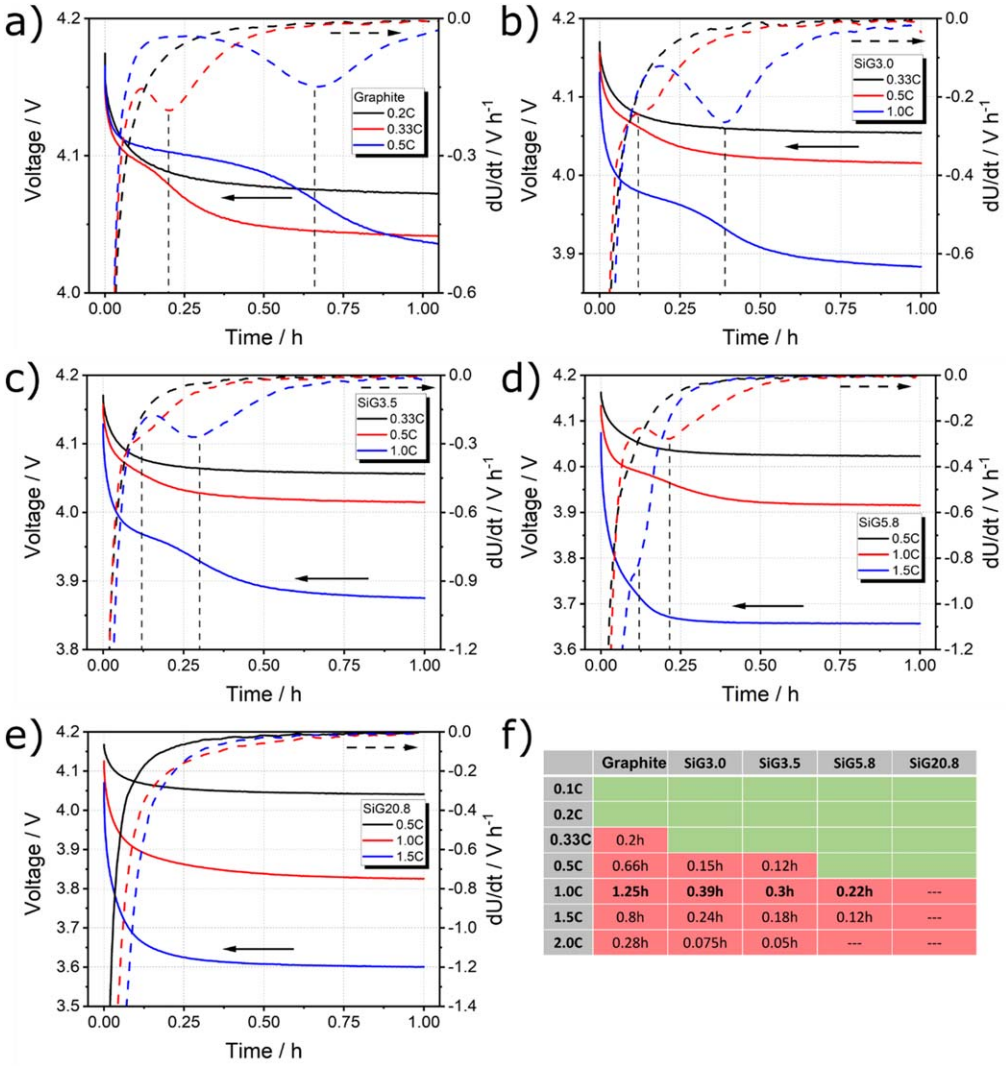

f)

	Graphite	SiG3.0	SiG3.5	SiG5.8	SiG20.8
0.1C					
0.2C					
0.33C	0.2h				
0.5C	0.66h	0.15h	0.12h		
1.0C	**1.25h**	**0.39h**	**0.3h**	**0.22h**	---
1.5C	0.8h	0.24h	0.18h	0.12h	---
2.0C	0.28h	0.075h	0.05h	---	---

Figure 4. (a)–(e) Voltage curves during the rest step after fast charging (solid line) are shown for the highest uncritical C-Rate (black), the critical C-rate (red) and the next highest C-rate tested (blue). The first derivative of the voltage curves are shown in dashed lines. (f) The matrix illustrates for each anode whether Li plating occurs (red) or whether no Li re-intercalation was detected (green). The values correspond to the duration until Li re-intercalation is completed.

using Eqs. (1) and (2). We noticed a linear relationship between the Si capacity share and the irreversible capacity losses, which is shown in Fig. 2f. This allows calculating the irreversible capacity losses of the anode with any Si content between 0 wt% and 20.8 wt%.

$$Q_{total} = \omega_{Gr} \cdot q_{Gr} + \omega_{Si} \cdot q_{Si} = Q_{Gr} + Q_{Si} \quad [1]$$

$$\frac{Q_{Si}}{Q_{total}} = \frac{Q_{total} - Q_{Gr}}{Q_{total}} \quad [2]$$

In these equations, ω is the mass fraction, q_{Gr} and q_{Si} are the experimental specific capacities of graphite and Si.

Anodes with different Si contents were coated with areal capacities in the narrow range of 3.25 mAh cm^{-2} ± 0.15 mAh cm^{-2}. At such constant areal capacity the anode coating thickness decreases with increasing Si content. Figures 2a–2e show the SEM cross-sections at the same magnification of the five anodes and the anode coating thickness clearly decreases. In these SEM image, Si particles are shown in a brighter shade of grey due to their higher atomic mass. Further, there is a linear relationship between the anode thickness and the Si capacity contribution, which is also shown in Fig. 2f.

It must be noted that thinner anode coatings will lead to larger electrode surface areas in a given cell volume. For example, in 21700 cells, the jellyrolls will then have additional windings.[43] Since larger electrode areas lower the cell impedance,[44] thinner electrodes as achieved by increasing Si content, could lead to cells with lower impedance and therefore to benefits of such cells in view of fast charging/discharging.

Based on the reversible and irreversible capacities of the anode and cathode active materials, we targeted a N/P ratio of 1.10. Cathode loading (mg cm^{-2}), and therefore cathode areal capacity (mAh cm^{-2}), was adjusted in order to compensate for the different irreversible capacity losses of anodes, hence having full-cells with a similar N/P ratio of 1.1. Details on the cathode and anode loadings are given in Table I. Table II shows that all the N/P ratios are very similar and therefore the cells are suitable for further experiments. This cell design results in anodes with identical areal capacity and therefore the same amount of Li inventory being in the cell. In addition, all anodes have a similar porosity and tortuosity. Therefore, any differences in the occurrence of Li plating on the anodes are solely due to different anode thicknesses resulting from the different Si contents.

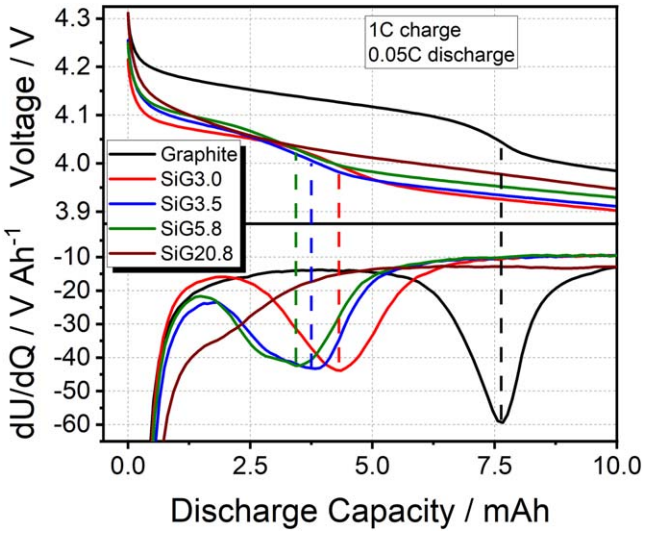

Figure 5. Stripping discharge experiment showing the voltage curve during discharge and the first derivative of the voltage vs the discharge capacity. The minimum in the first derivative marks the end of the stripping of deposited Li and the beginning of de-lithiation of the anode.

Fast-charging capability and low temperature charging.—Cells with different Si contents in the anodes were subjected to fast charging experiments at ambient temperatures of 25 °C as well as 0 °C. Charging was carried out in CC mode to observe potential Li re-intercalation during the voltage relaxation during resting-time after charging, which may have been masked by the CV phase. Charge rate capability tests for graphite were separately done with both available electrolytes to exclude any effect of the VC or FEC,[45–47] which are added as electrolyte additives to form a stable SEI on graphite and Si, respectively.

Figure 3a shows the charge rate capability at 25 °C, in which all cells were charged three times at each individual C-rate. Starting after 1 C charging, a C/10 check-up cycle between each C-rate was included to observe irreversible capacity losses. Until a charging rate of 1 C, little differences in the capacity retention were observed between the different cell types. The capacity retention at 1 C is close to 90%, most likely due to the low anode density of 1.3 g cm^{-3}, which facilitates fast diffusion pathways. From a C-rate of 1 C, the SiG20.8 cell type shows a lower capacity retention than the other cell types with lower Si content. Furthermore, high irreversible losses of SiG20.8 are already visible in the first check-up cycle. At even higher C-rates, the capacity retention further decreases and the irreversible losses continue to grow. SiG5.8 also shows lower capacity retention and higher irreversible losses compared to cells with a lower Si content. Even though the anode thickness decreases due to the higher Si content, cells with high Si content showed the lowest capacity retention. This result indicates, that Si is not beneficial towards the charge rate capability, most likely due to higher diffusion barriers of Li in Si (0.47–0.62 eV)[48–52] compared to Li diffusion in lithiated graphite (~0.2–0.4 eV).[53,54] However, we note that barriers are to best of our knowledge only available for single Li atoms in Si and not for higher lithiated alloys. This result indicates that the anode thickness is not the limiting factor for fast charging capability. Since the porosity in all anodes is very high, the better kinetics of the graphite most likely dominate. Irreversible capacity losses in the graphite cell and cells with Li contents of 3.0 wt% and 3.5 wt% firstly occurred after charging at 2 C. Deposition of Li on the anode surface of each cell type was confirmed by visual inspection after cell opening during the Post-Mortem analysis.

At 25 °C (Fig. 3a), the graphite cells with VC as electrolyte additive show better capacity retentions compared to graphite cells with FEC. In addition, the graphite cells containing FEC suffer from higher irreversible losses at high C-rates. However, at 0 °C the FEC containing graphite cells have a much better capacity retention compared to graphite cells with VC (Fig. 3b). Those findings are in agreement with literature, as VC as electrolyte additive was reported to increase the coulombic efficiency and cycle life of graphite based cells.[47] However, it also increases the charge transfer resistance of graphite anodes,[47] making it less suitable for fast charging, especially at low temperatures. FEC instead of VC was used as electrolyte additive for Si containing cells, as FEC forms a more flexible SEI.[45,46]

Figure 3b indicates that the Graphite (FEC) and SiG20.8 cell type, which had the lowest fast charging capability at 25 °C, shows the highest fast charging capability at 0 °C. In addition, SiG20.8 has the lowest irreversible capacity losses, which is obvious during the 0.1 C check-up cycle. Up to 1.5 C, Graphite (FEC) has the highest capacity retention, though from 1.5 C it decreases with every cycle. The capacity retention of the check-up cycles decreases most likely due to irreversible Li plating.

Cells with Si contents between 3.0 wt% and 5.8 wt% have the lowest capacity retention of all FEC containing cells at 0 °C. The capacity retention of these three cell types are too close in order to identify any trend related to Si content. The superior performance of graphite suggests that at low temperatures, lithiation of graphite is faster than the lithiation of Si (see discussion on Li diffusion barriers above). In addition, the stable capacity retention of SiG20.8 at 0 °C, which does not exhibit any irreversible capacity loss indicates that the reduction of the anode thickness by the addition of Si has a pronounced positive effect to the fast charging capability.

Reversible Li plating on the anode surface caused by fast charging can be observed during the rest step, since the re-intercalation of deposited Li into the anode causes a voltage plateau.[28,33,34,55,56] After each charging step, cells were given 1 h—3 h rest time for voltage relaxation. The cell voltage was differentiated versus time to determine the end of re-intercalation into the anode[33] in Figs. 4a–4e.

Cells tested at 25 °C exhibited visible Li deposition on the anode surface after cell opening, which was found during the Post-Mortem analysis, however, no voltage plateau was observed during voltage relaxation at this temperature. The amount of reversibly deposited Li might be either too small to detect, it re-intercalates too quickly into the anode, or it potentially reacts with the electrolyte instead of re-intercalating at 25 °C.

At 0 °C higher amounts of Li plating, as well as slowed down re-intercalation into graphite and reaction with the electrolyte can be expected compared to 25 °C. Such differences between the five different cell types were observed during the voltage relaxation at 0 °C (Fig. 4). Superior performance of the graphite cell with FEC as electrolyte additive compared to VC was decisive to study only the voltage relaxation of the graphite cell with FEC.

Voltage relaxation was used to determine a critical C-rate at which Li plating was observed for the first time. Figure 4 shows the voltage profiles in red color and its derivatives after charging at the critical C-rate, the next highest C-rate in blue color and the highest uncritical C-rate in black. Figure 4f summarizes the results of a total of 105 voltage relaxation measurements from Figs. 4a–4e. The matrix in Fig. 4f displays the critical C-rates in red and shows the time span, after which re-intercalation is completed.

Interestingly, the graphite cells already exhibit reversible Li plating at 0.33 C, although they have excellent fast charging behavior up to 1 C without irreversible capacity losses. Re-intercalation is completed after 0.2 h at 0.33 C, after 0.66 h at 0.5 C and not until 1.25 h at 1 C. At even higher C-rates, the re-intercalation time decreases, indicating that due to high overpotentials, the cut-off voltage is reached faster and less Li is deposited on the anode surface.

In Si containing cells reversible Li plating occurs at higher C-rates. For SiG3.0 and SiG3.5, which have Si contents of 3 wt% and 3.5 wt% respectively, the critical C-rate for Li-plating is 0.5 C. Re-intercalation time slightly decreases form SiG3.0 to SiG3.5,

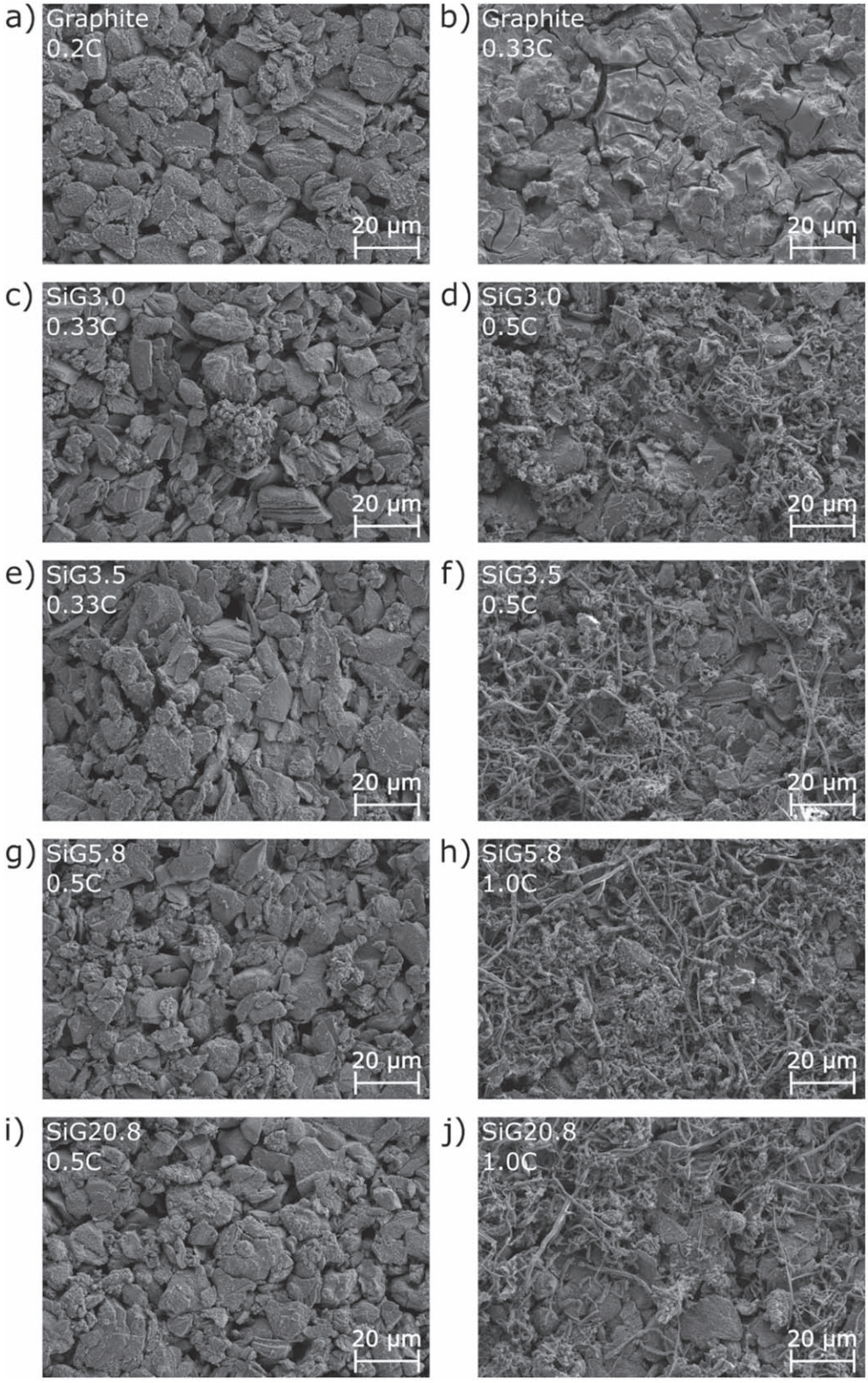

Figure 6. SEM images of the anodes after aging at the highest uncritical C-rate (left column) and the lowest critical C-rate (right column). Li plating was only measurable after aging at a critical C-rate.

indicating that less Li was deposited on the anode of SiG3.5 (compare Figs. 4b, 4c) The SiG5.8 cell type, which contains 5.8 wt% Si in the anode, first shows reversible Li plating at 1 C (Fig. 4d). In each of these four cell types (Graphite, SiGr3.0, SiGr3.5, SiG5.8), the maximum re-intercalation time is observed after charging at 1 C. In contrast, no voltage plateau could be observed in the relaxation profiles of SiG20.8. Post-Mortem analysis, however, proved that irreversible Li plating occurs as early

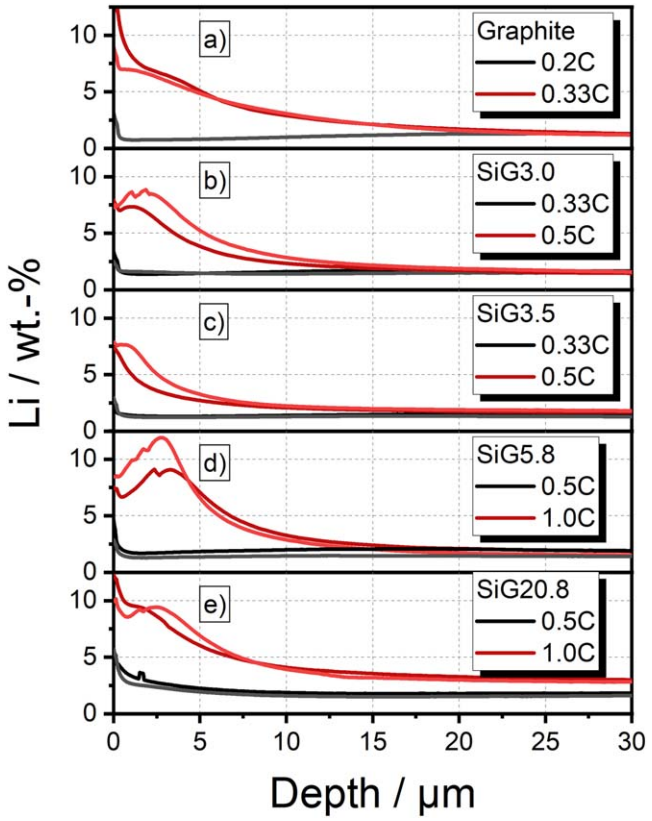

Figure 7. GD-OES measurements of the anodes aged at the highest uncritical C-rate (black and gray) and the critical C-rate (red and orange) show that the Li concentration on the anode surface is increased after critical aging. The graphs in a lighter shade show the reproduced measurements.

as 1 C for the cells with SiG20.8 anodes. Therefore, these fields in the matrix in Fig. 4f are marked red, pointing out that Li plating already occurred.

We clearly observed a trend towards higher critical C-rates for Li plating with higher Si contents (Fig. 4f). Based on this observation, the minimum in an Arrhenius plot of aging rates[57–60] will most likely shift to lower temperatures with higher Si content.

Additionally, the stripping discharges of the cells can be compared.[61–63] For this purpose, the cells were charged at 0 °C with constant current and immediately afterwards discharged at a low rate of 0.05 C (Fig. 5). The capacity charged into the cells at each C-rate is equal to the capacity charged into the cells at 0.1 C (CC) to 4.2 V. Thereby, it was ensured that the same capacity was charged into the cells at each C-rate. The mixed potential of plated Li and lithiated graphite and Si leads to a plateau in the discharge curve.[61] The minimum in the derivative of the voltage curve is caused by the voltage drop as the dissolution of deposited Li (Li stripping) is completed (Fig. 5).[63] Table III lists the amount of charge which originates from the stripping of deposited Li.

Reversible Li plating on graphite anodeswas first detected after charging at a C-rate between 0.2 C and 0.33 C, as was observed with voltage relaxation. In contrast, SiG3.0 to SiG5.8 first show Li stripping at charging C-rates between 0.33 C and 0.5 C. On the anode with the highest Si content (SiG20.8), no voltage plateau could be observed during stripping discharge.

With higher C-rates, the amount of Li that is stripped from the anode increases. However, the amount of Li that is stripped from Si/graphite anodes decreases with higher Si content.

The results from Fig. 5 show that with higher Si content, less Li is plated on the anode. In addition, the measurements are consistent with voltage relaxation experiments (Fig. 4), where the re-intercalation time, and thus most likely the amount of plated Li, decreases with higher Si content.

In this section, we primarily focused on Li plating at 0 °C. We have seen that although graphite cells have the best fast charging capability, they suffer from Li plating at lower C-rates at 0 °C. The cells become more tolerant to higher charging C-rates with higher Si content without showing Li plating. Additionally, the amount of Li plating at the same C-rate seems to decrease with higher Si content, i.e. with thinner anode coatings for very similar anode areal capacities, porosity, tortuosity, and N/P ratios.

Post-Mortem analysis of cells to detect Li plating.—Post-Mortem methods were applied to investigate whether Li fully re-intercalates into the anode materials or if Li is also deposited irreversibly as Li metal. For this reason, an aging procedure of five cycles at 0 °C at the respective critical C-rate and highest uncritical C-rate was started, before these cells were opened and investigated with SEM and GD-OES depth profiling. The critical C-rate refers to the charging C-rate, at which reversible Li deposition was observed in the voltage relaxation profile at 0 °C after fast-charging, whereas no re-intercalation could be observed after charging at an uncritical C-rate. SEM can detect the presence of Li deposits on the anode surface facing the separator,[38,39] while GD-OES depth profiling is used to create quantitative element profiles to determine the Li amount at the anode surface.[13,37] The aging procedure was deliberately kept short to avoid thick Li coverage of the anode surface, which would have impeded the GD-OES measurements.

SEM measurements of anodes in Fig. 6 display anodes after uncritical aging in the left column and after critical aging in the right column. The respective charging C-rates during aging are shown in the upper left corner. These SEM images confirm the electrochemical findings that no Li is deposited reversibly or irreversibly on the anode surface below the critical charging C-rate. In contrast, either a thick film (Fig. 6b) or dendrites (Figs. 6d, 6f, 6h) are evident on aged anodes cycled at the critical charging C-rates. This is fully consistent with the voltage relaxation experiments of Fig. 4.

In addition to the SEM images, GD-OES measurements were performed to detect Li plating on the anode surfaces. Figure 7 shows GD-OES depth profiles where a depth of 0 µm corresponds to the beginning of the measurements and therefore to the anode surface. Again, no Li plating was observed on the anode surfaces after aging at the highest uncritical C-rate. However, aging at the critical C-rate leads to a distinct increase of the Li concentration at the anode surface after only five cycles. The finding that Li plating happens mainly on the anode surface is consistent with previous GD-OES depth profiling studies with graphite[37] and Si/graphite [15,23] anodes, in situ optical microscopy experiments[64] from our group and simulations by Latz's group.[65,66] We noticed that compared to our previous GD-OES measurements mostly using strongly aged cells, Li plating can also be detected after few aging cycles.

Li plating detected with SEM and GD-OES arises from irreversibly deposited Li, while voltage relaxation and stripping discharge detects reversible deposited Li. The observation of irreversibly lost Li demonstrates that the deposited Li does not re-intercalate completely but undergoes side-reactions or must have lost electrical contact to the anode. Overall, the critical C-rates found by GD-OES in Fig. 7 are fully consistent with the SEM measurements in Fig. 6 and with the voltage relaxation curves in Fig. 4. These results are also mostly consistent with those from the Li stripping experiments in Fig. 5. The only deviation was found in case of SiG20.8 where Li plating was not evident in the voltage relaxation curves.

In order to assess the Li deposition behavior on the anodes at 23 °C, half cells were opened immediately after charging and investigated with high-resolution light microscopy under inert gas atmosphere (Fig. 8). The anodes graphite, SiG3.0, SiG5.8 and SiG20.8 were charged in half cell setup at 1 C to 50%, 60%, 70%, 80%, 90%, and 100% SOC and the presence of Li depositions was compared. Due to the very similar Si content of the anodes SiG3.0 and SiG3.5, only the anode SiG3.0 was investigated with ex situ microscopy. The short time-span of 2 min between end of charging and cell opening and the fast evaporation of the electrolyte most likely prevent the re-intercalation of Li into the anode.

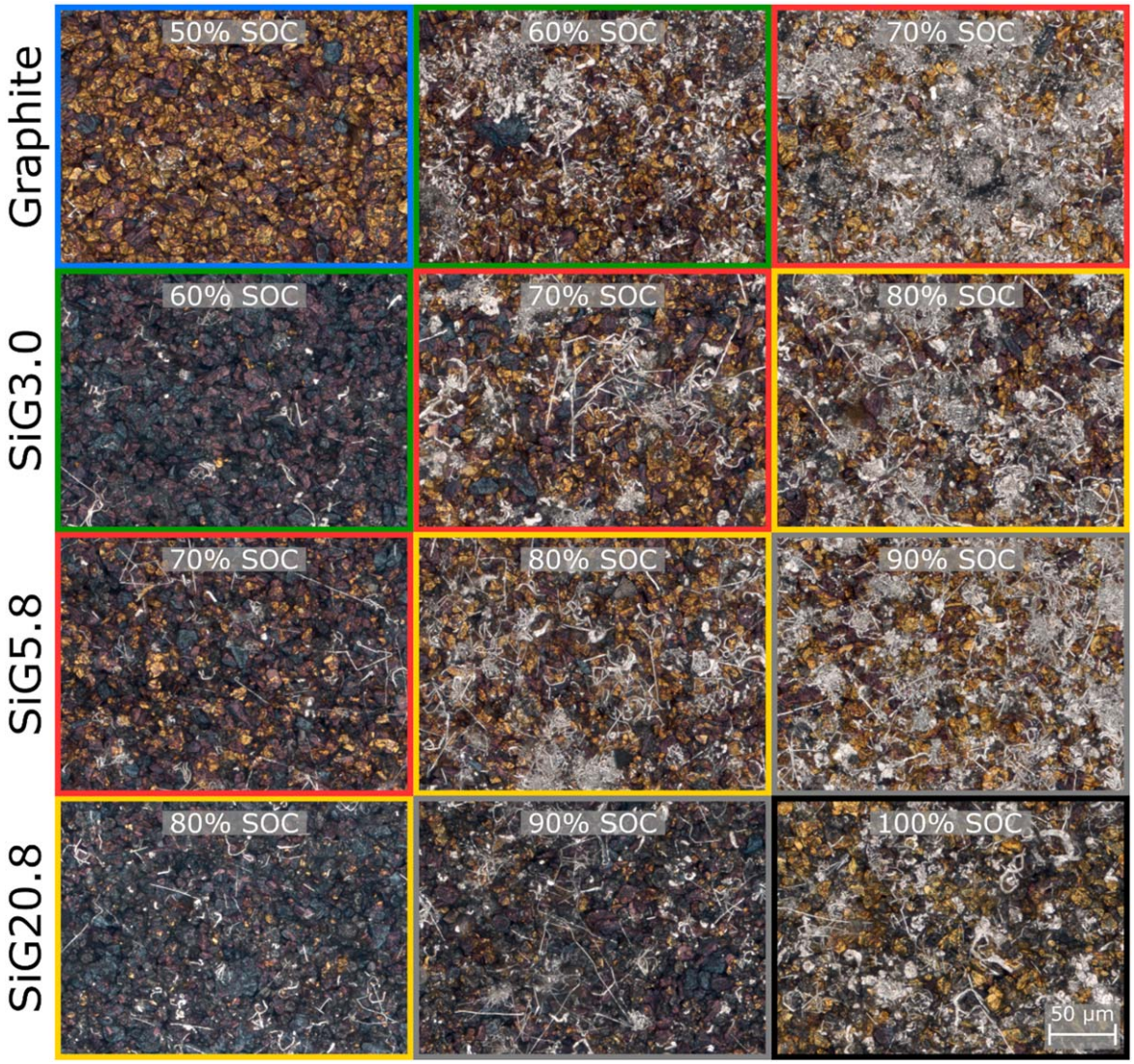

Figure 8. Light microscopy images of the anode surfaces at different SOCs. The images show that with increasing Si content the SOC, at which Li is deposited on the anode surface, increases.

Figure 8 includes images of each anode at three different SOCs, at which Li deposition is hardly visible (left column), locally visible (middle column) or covering the anode surface (right column). Images at the same SOC are framed by the same color. A general trend was observed toward higher SOC to observe more Li on the anode surface.

Li deposition on graphite anodes first appeared at 50% SOC and at 70% SOC the anode surface was fully covered with Li. The anode SiG3.0 showed isolated Li dendrites at 60% SOC, however, at 70% SOC the amount of Li dendrites has increased significantly. Similarly, the anode SiG5.8 exhibited Li plating at 80% SOC, however, few Li dendrites were already visible at 70% SOC. Full coverage of the anode SiG20.8 was only visible at 100% SOC, with local Li deposits already visible at 90% SOC. These findings demonstrate that also at ambient temperatures Li plating is less pronounced with increasing Si content. This trend is consistent with the results obtained at 0 °C using voltage relaxation and stripping discharge.

Conclusions

We investigated the effect of Si content in anodes on their susceptibility to Li plating. Therefore, five types of anodes with different Si contents and corresponding cathodes were coated on pilot scale. The anode areal capacities were kept constant to reduce the anode coating thickness for anodes with higher Si contents. The areal capacity of the cathodes were tailored to compensate the irreversible capacity losses of the anodes and to obtain pouch full cells with different Si contents and very similar N/P ratios. Furthermore, the porosity and tortuosity of the anodes were almost identical, so that their influence could be excluded. We observed a linear relationship between the Si capacity contribution to the total anode capacity and the irreversible capacity losses of the anodes during the three formation cycles.

The fast charging performance of all cells was compared in charge rate capability tests at 25 °C and 0 °C. We found that at 25 °C cells with low Si content and the graphite cell filled with VC containing electrolyte performed best. The capacity retention declined with increasing Si content. At 0 °C, however, the cell with the highest Si content along with the graphite cell filled with FEC containing electrolyte have the highest capacity retention at the highest C-rate. Lower Si contents have a lower capacity retention indicating that the reduction of the anode thickness is most beneficial for the charge rate capability.

Voltage relaxation experiments after charging at 0 °C were conducted to detect reversible Li plating at 0 °C. For each cell type except SiG20.8 a critical C-rate was found, at which reversible Li plating could be detected for the first time. The critical C-rate increases with Si-content, making cells with high Si content at similar areal capacity and therefore thinner anodes more resistant to Li plating at low temperatures.

A short aging procedure at 0 °C followed by Post-Mortem analysis with GD-OES and SEM was carried out to determine if irreversible Li plating occurs at the critical C-rate. Consistent with operando methods, Li plating has been detected at the critical C-rate, however, no Li plating occurs below the critical C-rate. Voltage relaxation, Li stripping, SEM measurements and GD-OES depth profiling are validated against each other and revealed clear trends on the susceptibility of Si/graphite anodes at 0 °C for the same anode areal capacities with Si increasing content.

Optical microscopy under inert gas atmosphere was used to investigate the presence of Li deposition at defined SOC levels. Similarly, the same trend as found at 0 °C, that high Si contents and thus thinner anodes make the cells more resistant to Li plating, was also found at 23 °C.

Overall, our results clearly showed that Si compounds in graphite anodes can have a positive effect by hindering Li plating, however, they can also increase the aging rate at 25 °C. The Si content will most likely shift the temperature of the minimum aging rate in Arrhenius plots. The thinner electrode coatings arising from Si in the anodes will furthermore decrease the impedance of battery cells, e.g. by additional available electrode surface in a given battery cell size. Further experiments into these directions are ongoing in our labs.

Acknowledgments

Funding of the project CharLiSiKo (AQua-Cluster) by the German Federal Ministry of Education and Research (BMBF) under contract n° 03XP0333A and project management by Projektträger Jülich (PTJ) are gratefully acknowledged. The authors are indebted to the ZSW members C. Pfeifer for SEM/EDX, G. Arnold for ICP-OES measurements, K. Fischinger for Hg porosimetry measurements, as well as M. Feinauer (ZSW) and C. Weisenberger (AU) for fruitful discussions.

ORCID

Marius Flügel https://orcid.org/0000-0002-9792-0414
Mario Marinaro https://orcid.org/0000-0002-5954-0357
Thomas Waldmann https://orcid.org/0000-0003-3761-1668

References

1. J. R. Dahn, T. Zheng, Y. Liu, and J. S. Xue, *Science*, **270**, 590 (1995).
2. F. Luo, B. Liu, J. Zheng, G. Chu, K. Zhong, H. Li, X. Huang, and L. Chen, *J. Electrochem. Soc.*, **162**, A2509 (2015).
3. L. Y. Beaulieu, T. D. Hatchard, A. Bonakdarpour, M. D. Fleischauer, and J. R. Dahn, *J. Electrochem. Soc.*, **150**, A1457 (2003).
4. J. Li, A. K. Dozier, Y. Li, F. Yang, and Y.-T. Cheng, *J. Electrochem. Soc.*, **158**, A689 (2011).
5. X. H. Liu, L. Zhong, S. Huang, S. X. Mao, T. Zhu, and J. Y. Huang, *ACS Nano*, **6**, 1522 (2012).
6. Y. Wang, Y. Liu, J. Zheng, H. Zheng, Z. Mei, X. Du, and H. Li, *Nanotechnology*, **24**, 424011 (2013).
7. Y. Hu, B. Yu, X. Qi, B. Shi, S. Fang, Z. Yu, and J. Yang, *J. Mater. Sci.*, **55**, 10155 (2020).
8. W. An, B. Gao, S. Mei, B. Xiang, J. Fu, L. Wang, Q. Zhang, P. K. Chu, and K. Huo, *Nat. Commun.*, **10**, 1447 (2019).
9. S. Y. Kim, J. Lee, B.-H. Kim, Y.-J. Kim, K. S. Yang, and M.-S. Park, *ACS Appl. Mater. Interfaces*, **8**, 12109 (2016).
10. H. Jia, X. Li, X. Zhang, L. Luo, Y. He, B. Li, Y. Cai, S. Hu, X. Xiao, C. Wang, K. Rosso, R. Yi, R. Patel, and J.-G. Zhang, *Nat. Commun.*, **11**, 1474 (2020).
11. P. Kuntz, O. Raccurt, P. Azaïs, K. Richter, T. Waldmann, M. Wohlfahrt-Mehrens, M. Bardet, A. Buzlukov, and S. Genies, *Batteries*, **7**, 48 (2021).
12. B. Lain, J. Brandon, and E. Kendrick, *Batteries*, **5**, 64 (2019).
13. K. Richter, T. Waldmann, M. Kasper, C. Pfeifer, M. Memm, P. Axmann, and M. Wohlfahrt-Mehrens, *J. Phys. Chem. C*, **123**, 18795 (2019).
14. K. Richter, T. Waldmann, M. Memm, M. Kasper, and M. Wohlfahrt-Mehrens, *J. Electrochem. Soc.*, **165**, A3602 (2018).
15. M. Flügel, K. Richter, M. Wohlfahrt-Mehrens, and T. Waldmann, *J. Electrochem. Soc.*, **169**, 50533 (2022).
16. M. Schindler, J. Sturm, S. Ludwig, A. Durdel, and A. Jossen, *J. Electrochem. Soc.*, **168**, 60522 (2021).
17. J. Schmitt, M. Schindler, and A. Jossen, *J. Power Sources*, **506**, 230240 (2021).
18. D. Anseán, G. Baure, M. González, I. Cameán, A. B. García, and M. Dubarry, *J. Power Sources*, **459**, 227882 (2020).
19. K. Kalaga, M.-T. F. Rodrigues, S. E. Trask, I. A. Shkrob, and D. P. Abraham, *Electrochim. Acta*, **280**, 221 (2018).
20. X. Li, A. M. Colclasure, D. P. Finegan, D. Ren, Y. Shi, X. Feng, L. Cao, Y. Yang, and K. Smith, *Electrochim. Acta*, **297**, 1109 (2019).
21. T. Waldmann, N. Ghanbari, M. Kasper, and M. Wohlfahrt-Mehrens, *J. Electrochem. Soc.*, **162**, A1500 (2015).
22. A. Iturrondobeitia, F. Aguesse, S. Genies, T. Waldmann, M. Kasper, N. Ghanbari, M. Wohlfahrt-Mehrens, and E. Bekaert, *J. Phys. Chem. C*, **121**, 21865 (2017).
23. K. Richter, T. Waldmann, N. Paul, N. Jobst, R.-G. Scurtu, M. Hofmann, R. Gilles, and M. Wohlfahrt-Mehrens, *ChemSusChem*, **13**, 529 (2020).
24. T. Waldmann, B.-I. Hogg, and M. Wohlfahrt-Mehrens, *J. Power Sources*, **384**, 107 (2018).
25. Y. Jiang et al., *Energy Storage Mater.*, **28**, 17 (2020).
26. T. Yang, Y. Sun, T. Qian, J. Liu, X. Liu, F. Rosei, and C. Yan, *Energy Storage Mater.*, **26**, 385 (2020).
27. T. Waldmann and M. Wohlfahrt-Mehrens, *Electrochim. Acta*, **230**, 454 (2017).
28. T. Waldmann, J. B. Quinn, K. Richter, M. Kasper, A. Tost, A. Klein, and M. Wohlfahrt-Mehrens, *J. Electrochem. Soc.*, **164**, A3154 (2017).
29. Y. Tian, C. Lin, H. Li, J. Du, and R. Xiong, *Appl. Energy*, **300**, 117386 (2021).
30. Z. Li, J. Huang, B. Yann Liaw, V. Metzler, and J. Zhang, *J. Power Sources*, **254**, 168 (2014).
31. S. S. Zhang, K. Xu, and T. R. Jow, *J. Power Sources*, **160**, 1349 (2006).
32. T. Waldmann, B.-I. Hogg, M. Kasper, S. Grolleau, C. G. Couceiro, K. Trad, B. P. Matadi, and M. Wohlfahrt-Mehrens, *J. Electrochem. Soc.*, **163**, A1232 (2016).
33. C. von Lüders, V. Zinth, S. V. Erhard, P. J. Osswald, M. Hofmann, R. Gilles, and A. Jossen, *J. Power Sources*, **342**, 17 (2017).
34. S. Schindler, M. Bauer, M. Petzl, and M. A. Danzer, *J. Power Sources*, **304**, 170 (2016).
35. N. Legrand, B. Knosp, P. Desprez, F. Lapicque, and S. Raël, *J. Power Sources*, **245**, 208 (2014).
36. D. Aurbach, I. Weissman, A. Schechter, and H. Cohen, *Langmuir*, **12**, 3991 (1996).
37. N. Ghanbari, T. Waldmann, M. Kasper, P. Axmann, and M. Wohlfahrt-Mehrens, *J. Phys. Chem. C*, **120**, 22225 (2016).
38. H. Honbo, K. Takei, Y. Ishii, and T. Nishida, *J. Power Sources*, **189**, 337 (2009).
39. A. Friesen, F. Horsthemke, X. Mönnighoff, G. Brunklaus, R. Krafft, M. Börner, T. Risthaus, M. Winter, and F. M. Schappacher, *J. Power Sources*, **334**, 1 (2016).
40. E. Moyassari, T. Roth, S. Kücher, C.-C. Chang, S.-C. Hou, F. B. Spingler, and A. Jossen, *J. Electrochem. Soc.*, **169**, 10504 (2022).
41. M. Jiao, Y. Wang, C. Ye, C. Wang, W. Zhang, and C. Liang, *J. Alloys Compd.*, **842**, 155774 (2020).
42. Y. Jiang, G. Offer, J. Jiang, M. Marinescu, and H. Wang, *J. Electrochem. Soc.*, **167**, 130533 (2020).
43. T. Waldmann, R.-G. Scurtu, K. Richter, and M. Wohlfahrt-Mehrens, *J. Power Sources*, **472**, 228614 (2020).
44. T. Waldmann, S. Rössler, M. Blessing, R. Schäfer, R.-G. Scurtu, W. Braunwarth, and M. Wohlfahrt-Mehrens, *J. Electrochem. Soc.*, **168**, 090519 (2021).
45. E. Markevich, G. Salitra, and D. Aurbach, *ACS Energy Lett.*, **2**, 1337 (2017).
46. C. Xu, F. Lindgren, B. Philippe, M. Gorgoi, F. Björefors, K. Edström, and T. Gustafsson, *Chem. Mater.*, **27**, 2591 (2015).
47. J. C. Burns, R. Petibon, K. J. Nelson, N. N. Sinha, A. Kassam, B. M. Way, and J. R. Dahn, *J. Electrochem. Soc.*, **160**, A1668 (2013).
48. H. Kim, K. E. Kweon, C.-Y. Chou, J. G. Ekerdt, and G. S. Hwang, *J. Phys. Chem. C*, **114**, 17942 (2010).
49. C.-Y. Chou, H. Kim, and G. S. Hwang, *J. Phys. Chem. C*, **115**, 20018 (2011).
50. O. I. Malyi, T. L. Tan, and S. Manzhos, *Appl. Phys. Express*, **6**, 27301 (2013).
51. W. Wan, Q. Zhang, Y. Cui, and E. Wang, *Journal of physics: Condensed matter*, **22**, 415501 (2010).
52. Z. Wang, Q. Su, H. Deng, W. He, J. Lin, and Y. Q. Fu, *J. Mater. Chem. A*, **2**, 13976 (2014).
53. K. Persson, V. A. Sethuraman, L. J. Hardwick, Y. Hinuma, Y. S. Meng, A. van der Ven, V. Srinivasan, R. Kostecki, and G. Ceder, *J. Phys. Chem. Lett.*, **1**, 1176 (2010).
54. K. Persson, Y. Hinuma, Y. S. Meng, A. van der Ven, and G. Ceder, *Phys. Rev. B*, **82**, 125416 (2010).
55. V. Zinth, C. von Lüders, M. Hofmann, J. Hattendorff, I. Buchberger, S. Erhard, J. Rebelo-Kornmeier, A. Jossen, and R. Gilles, *J. Power Sources*, **271**, 152 (2014).
56. C. Uhlmann, J. Illig, M. Ender, R. Schuster, and E. Ivers-Tiffée, *J. Power Sources*, **279**, 428 (2015).
57. T. Waldmann, M. Wilka, M. Kasper, M. Fleischhammer, and M. Wohlfahrt-Mehrens, *J. Power Sources*, **262**, 129 (2014).
58. X.-G. Yang and C.-Y. Wang, *J. Power Sources*, **402**, 489 (2018).
59. M. Bozorgchenani, G. Kucinskis, M. Wohlfahrt-Mehrens, and T. Waldmann, *J. Electrochem. Soc.*, **169**, 30509 (2022).
60. G. Kucinskis, M. Bozorgchenani, M. Feinauer, M. Kasper, M. Wohlfahrt-Mehrens, and T. Waldmann, *J. Power Sources*, **549**, 232129 (2022).
61. R. V. Bugga and M. C. Smart, *ECS Trans.*, **25**, 241 (2010).
62. C. von Lüders, J. Keil, M. Webersberger, and A. Jossen, *J. Power Sources*, **414**, 41 (2019).
63. M. Petzl and M. A. Danzer, *J. Power Sources*, **254**, 80 (2014).
64. C. Hogrefe, T. Waldmann, M. Hölzle, and M. Wohlfahrt-Mehrens, *J. Power Sources*, **556**, 232391 (2023).
65. S. Hein and A. Latz, *Electrochim. Acta*, **201**, 354 (2016).
66. T. Danner, M. Singh, S. Hein, J. Kaiser, H. Hahn, and A. Latz, *J. Power Sources*, **334**, 191 (2016).